



# Experimental measurements of the high-temperature oxidation of carbon fibers

Francesco Panerai<sup>a,\*</sup>, Thom Cochell<sup>b</sup>, Alexandre Martin<sup>c</sup>, Jason D. White<sup>d</sup>

<sup>a</sup>AMA Inc. at NASA Ames Research Center, Moffett Field, CA 94035, USA

<sup>b</sup>Department of Chemical and Materials Engineering, University of Kentucky, Lexington, KY 40506, USA

<sup>c</sup>Department of Mechanical Engineering, University of Kentucky, Lexington, KY 40506, USA

<sup>d</sup>SRI International, Menlo Park, CA 94025, USA

## ARTICLE INFO

### Article history:

Received 12 October 2018

Received in revised form 14 February 2019

Accepted 4 March 2019

Available online 18 March 2019

## ABSTRACT

We carried out laboratory experiments to study the decomposition of carbon fibers at high temperature and studied the material used in charring carbon phenolic ablators for planetary probe heatshields. Porous plug samples were exposed to controlled rates of molecular oxygen, carbon dioxide, and carbon monoxide at furnace-heated flow-tube reactor temperatures between 700 and 1500 K and pressures between 2000 and 6200 Pa. We used calibrated mass spectroscopy to make time-resolved quantitative measurements of decomposition products of the gases downstream of the test sample. Absolute and differential pressure measurements were used to determine the high-temperature permeability of the material and to monitor changes during material decomposition, and we characterized the microstructure of the porous sample using scanning electron microscopy. We found substantial carbon fiber oxidation for O<sub>2</sub> flows, resulting in increasing CO/CO<sub>2</sub> production ratios with increasing temperature. The CO<sub>2</sub> was shown to react with carbon fibers following a Boudouard reaction at temperatures above 1200 K.

© 2019 Elsevier Ltd. All rights reserved.

## 1. Introduction

Fibrous composites are used in many different applications as high-performance insulators. With pore fractions higher than ~80%, this class of materials effectively protects underlying structures from surrounding heat sources by providing a gaseous buffer at high temperatures. Examples of applications are diverse, including industrial furnaces [1], fire protection [2], batting materials [3], and heat shields of high-speed spacecraft [4]. Among other insulators, carbon fiber materials are an established technology for very high-temperature environments. Specifically, both rigid and flexible insulators have been used as substrates for carbon/phenolic ablators, serving as heat-shield materials for hypersonic entry [5,6]. Low-density materials provide optimal shielding with minimal added payload mass. FiberForm® (Fiber Materials, Inc., Biddeford, ME, USA) (FF) [4] is the focus of this work because it is the rigid fibrous preform of PICA (phenolic-impregnated carbon ablator) [5], a material used in the thermal protection systems (TPS) of several space exploration vessels [7,8]. The FF and PICA materials, among others, have been extensively demonstrated in both testing and operational environments [5,7,9–11].

Under operational conditions in oxygen-rich atmospheres, the carbon fibers of ablative heat-shield materials undergo both physical and chemical decomposition, which is most often seen under high-temperature oxidation conditions like those observed during atmospheric entry [12]. Most studies to date have focused on Earth's atmosphere. Recent decisions for future spaceflights have renewed interest in sending robotic and manned spacecraft to Mars, where the atmosphere is 96% CO<sub>2</sub> [13] and will impact the TPS differently than in terrestrial conditions. As such, our study explores the interaction of CO<sub>2</sub> and fibrous carbon material.

The design of optimal TPS materials requires modeling codes that account for the interaction of oxidizing species and the ablator. The current state-of-the-art design models calculate surface ablation rates by using non-dimensional surface energy balance tables [6] that assume chemical equilibrium at the fluid/solid interface [14–16]. Although these constitute a legitimate approximation, they fail to capture in-depth decomposition phenomena [17] and overestimate the ablation rate at low temperature and low heat fluxes [18]. This becomes an issue near the end of the trajectories, where the heat fluxes are less than 80 W/cm<sup>2</sup> and the surface temperatures below 1800 K. At such conditions, carbon ablation is no longer limited by boundary-layer diffusion; instead, it is limited by the surface kinetic rates. [15]. This inappropriate treatment of surface ablation leads to peculiar results such as the

\* Corresponding author.

E-mail address: [francesco.panerai@nasa.gov](mailto:francesco.panerai@nasa.gov) (F. Panerai).

**Nomenclature**

$d$	diameter, m
$F$	force, N
$K$	permeability, $\text{m}^2$
$L$	length, m
$m$	mass, g
$m/z$	mass-to-charge ratio
$\dot{m}$	mass flow, $\text{g s}^{-1}$
$M$	molar mass, $\text{g mol}^{-1}$
$p$	partial pressure, Pa
$P$	pressure, Pa
$\mathcal{R}$	universal gas constant, $8.3145 \text{ J mol}^{-1} \text{ K}^{-1}$
$t$	oxidation time, s
$T$	temperature, K

**Greek**

$\phi$	porosity
$\mu$	dynamic viscosity, Pa s
$\rho$	density, $\text{kg m}^{-3}$

**Subscripts**

0	initial or intrinsic
1	port 1 (upstream of the sample)
2	port 2 (downstream of the sample)
$avg$	average
$b$	base

$C$	carbon
$e$	end
$f$	furnace
$i$	related to $i$ -th species
$in$	inlet
$out$	outlet
$s$	sample

**Superscript**

$\dagger$	normalized
*	reference

**Acronyms**

BV	Ball Valve
IP	In-Plane
FF	FiberForm
PICA	Phenolic Impregnated Carbon Ablator
RGA	Residual Gas Analysis
SEM	Scanning Electron Microscopy
SLM	Standard Liter per Minute
TPS	Thermal Protection System
TC	Thermocouple
TPD	Temperature-Programmed Desorption
TT	Through-Thickness

so-called “end-game” phenomenon in which simulations predict a surface temperature increase instead of a cool down [19].

Past research efforts have addressed the limitations of surface equilibrium chemistry by using finite-rate surface models [20–22]. These works were followed by similar implementations using more detailed surface chemistry models based on literature data [23–30], or species-specific reaction rates derived from experiments [31–35]. The results using these models indicated that a rate-based surface approach could provide a path to significantly improve the understanding of the chemistry at the surface of porous ablators. These models, however, need to be validated in the context of high-temperature porous flow because the chemical interactions within porous materials are very different from those in a solid, homogeneous, reacting surface. More specifically, the interactions of the transported gas within the porous media and the available reactive surface are also much different [36,37].

Although many studies have been dedicated to quantifying carbon oxidation and gasification processes [37–45], the extraction of reactivities, rates, or reaction efficiencies for use in numerical models is an unsolved challenge [46]. The variability of decomposition processes with both the environmental conditions at which experiments are performed and the nature of the carbon material analyzed constitute major difficulties. Literature data on carbon oxidation show experimental values of reactivities under apparently similar conditions may differ by a factor of ten [10–13]. The major causes of these discrepancies are well known and include differences in carbon types, catalytic effects, differing thermal treatments for nominally similar material, and experimental variations in gas velocity, purity of the air, configuration of the reactor, and diffusion effects. The literature describing porous chars used in lightweight ablators is limited to a handful of experimental studies with insufficient results to provide a comprehensive validation database [47,48]. These studies are limited to air gas only and do not provide quantification of oxidation products.

In the present work, experiments were performed on the decomposition of FF with a nominal density of  $180 \text{ g/cm}^3 \pm 10\%$  and a porosity of  $0.87 \pm 0.05$  [47] at temperatures between 500 K and 1500 K. Cylindrical plug samples of FF were placed in the furnace-heated tubular reactor and subjected to controlled mass flow rates of pure molecular  $\text{O}_2$ ,  $\text{CO}_2$  and  $\text{CO}$  at temperatures up to  $\sim 1500 \text{ K}$ . We studied decomposition via oxidation using pressure and temperature measurements, in-situ mass spectroscopy of reaction products, and post-test characterizations of the material samples with scanning electron microscopy (SEM). For the purpose of developing chemical kinetics models, FF is an ideal choice because it is a thoroughly characterized material, with properties such as porosity, tortuosity and effective thermal conductivity that are well documented in the open literature [4,49,50].

## 2. Experiment

### 2.1. Setup and instrumentation

We assembled a high-temperature flow-tube setup (Fig. 1) to perform gas/material interaction experiments on porous carbon samples [47,51]. The system consisted of a 129.5-cm long, 22-mm inner diameter fused-quartz tube positioned inside of a high-temperature electric tube furnace that utilized a radiative silicon carbide heating element to provide temperatures up to  $\sim 1650 \text{ K}$ . Virgin, 20-mm long cylindrical plug samples of FF were press-fit in the tube [52]. This method enabled a tight seal of the plug against the wall of the tube, forcing the gas flow to pass through the porous material allowing for real-time pressure drop measurements. The FF was positioned in the center of the furnace using a dowel rod. Because of its manufacturing process, FF has a transverse isotropic microstructure (fibers preferentially aligned within a plane) that gives the material a lower through-thickness (TT) thermal conductivity compared to the in-plane (IP) conductivity. We used the TT orientation for all experiments, and gases were

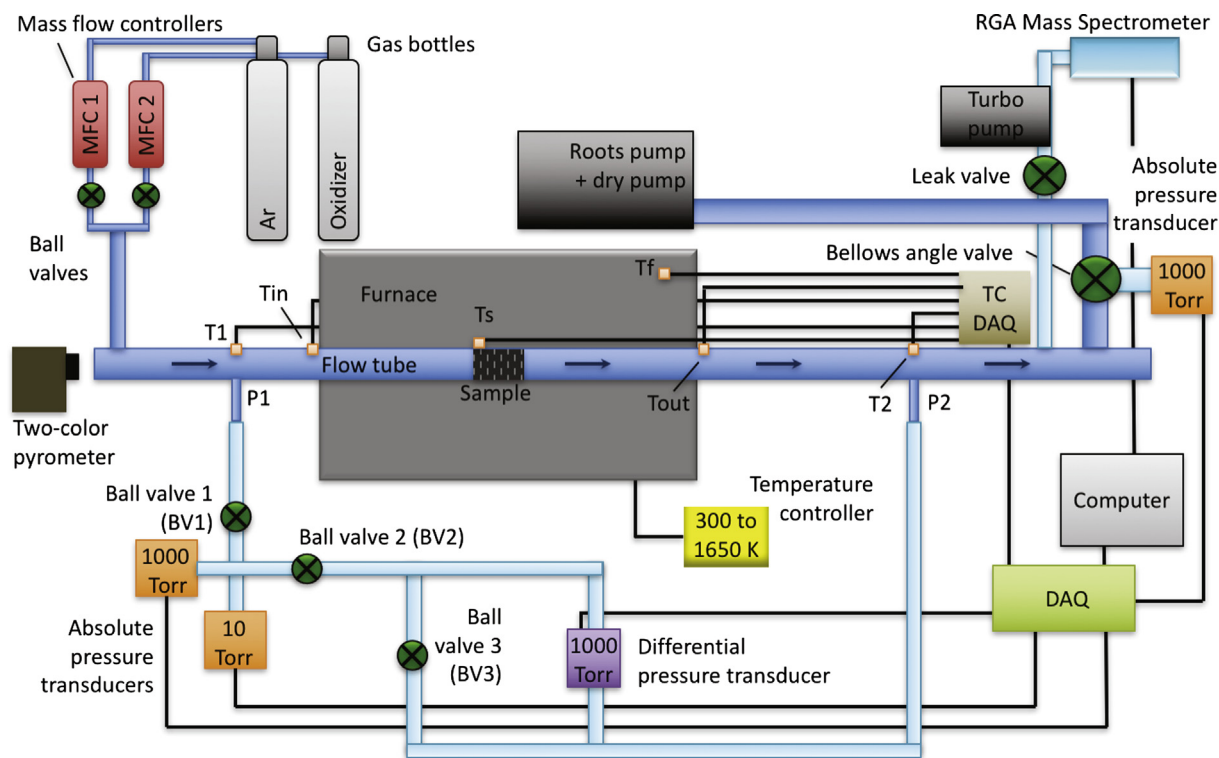


Fig. 1. Schematic of the flow-tube setup and instrumentation.

flowed normal to the plane of the fibers because the axial geometry of the porous material plays a major role in the material's permeability [51].

Gases of Ar (ultra-high purity grade 99.999%, Praxair Technology, Inc., San Francisco, CA, USA), O<sub>2</sub> (research grade 99.999%, Air-gas, Inc., Radnor, PA, USA), CO<sub>2</sub> (research purity 99.999%, Matheson Tri-Gas, Inc., Fremont, CA, USA) and CO (PurityPlus 4.0 Grade 99.99%, Alliance Welding Supplies, Inc., Oakland, CA, USA) were used. The experimental and calibration gases were controlled by a dedicated mass flow controller (UFC-8160, Unit Instruments, Inc., Orange, CA, USA), with flows set by a Tylan control box (RO-28, Tylan General, San Diego, CA, USA). Mass-flow calibration was carried out as described in the manual, and was corrected for the controller span and the calibration gas originally used for each specific controller (Ar: 1 SLM NF<sub>3</sub>, O<sub>2</sub>, 1 SLM H<sub>2</sub>, CO<sub>2</sub>: 1 SLM H<sub>2</sub>, CO: 1 SLM H<sub>2</sub>). Gas flow rates were 2.34, 2.27, and 2.06 mg s<sup>-1</sup> for O<sub>2</sub>, CO<sub>2</sub> and CO, respectively.

The outlet of the flow-tube was connected to the vacuum system through a manual bellows-angle valve that was fully opened during the experiments. The system was evacuated by means of a roots pump (Alcatel R301B, Alcatel Vacuum Technology, France) using Fomblin<sup>®</sup> oil and backed by a dry pump (Alcatel BF ADP 81, Alcatel Vacuum Technology, France). The pumping manifold was outfitted with a copper mesh and filter paper to protect the vacuum pump from particulates that might be generated during the experiment. Although the filter collected part of the fibers that shed off the FF sample during the test, it was determined that the collected material was not an accurate quantification of mass removed by spallation.

The quartz flow tube was equipped with ports upstream (P1) and downstream (P2) of the furnace to monitor pressure through a manifold of pressure transducers and a series of ball valves (BVs) to control the flow path. Two absolute capacitance manometers, one a 1000-Torr range (Baratron<sup>®</sup> 628, MKS instruments, Inc., Andover, MA, USA) and the other a 10-Torr range (Baratron<sup>®</sup> 122A,

MKS instruments, Inc., Andover, MA, USA), were installed to measure the absolute pressure either at P1 or P2, depending on the operating position of BV1 and BV2. Both absolute transducers and 1000-Torr differential pressure transducer (Baratron<sup>®</sup> 223B, MKS instruments, Inc., Andover, MA, USA) were used to measure the pressure differential ( $P_1 - P_2$ ) across the sample. In normal operation, BV3 was closed, allowing the differential pressure gauges to operate and forcing the flow through the porous plug. A redundant absolute pressure measurement was taken downstream of the sample, using an additional 1000-Torr absolute capacitance manometer (Baratron<sup>®</sup> 227A, MKS instruments, Inc., Andover, MA, USA) installed at the exit of the tube.

Thermocouple (TC) sensors were installed at various positions along the tube as depicted in Fig. 1. Two type-K thermocouples were used to measure the temperatures,  $T_1$  and  $T_2$ , at the pressure ports, P1 and P2, respectively, and two other type-K TCs monitored the temperatures,  $T_{in}$  and  $T_{out}$ , at the inlet and outlet of the furnace. A type-S TC and type-K TC were used to measure the temperature of the sample  $T_s$  and the temperature of the furnace  $T_f$ , respectively. The type-S thermocouple was placed in contact with the quartz tube near the upstream face of the sample, while the type-K was placed about 5 cm upstream of the furnace outlet in the vicinity of the quartz tube. A two-color pyrometer (Mikron M90-R2, LumaSense Technologies, Inc., Santa Clara, CA, USA) directed toward the upstream surface of the sample was also used as a redundant temperature measurement for the tests at temperatures above 1200 K. All of these temperature measurements agreed within  $\pm 10$  K.

All temperature and pressure measurements were acquired at 4-s intervals using a dedicated acquisition card (NI Model USB-6210, National Instrument, Austin, TX, USA). A customized Lab-View interface recorded each parameter directly to a computer and enabled real-time monitoring of the data. Thermocouple signals were also recorded by a 16-channel thermocouple monitor (SR630, Stanford Research System, Inc., Sunnyvale, CA, USA), and

pressure data were displayed on a dedicated power supply readout systems (MKS PDR-C-1C, MKS Instruments, Inc., Andover, MA, USA).

The specimens were characterized before and after oxidation using a digital caliper to measure length and diameter, a high-precision scale (B5, Mettler-Toledo, LLC, Columbus, OH, USA) with  $\pm 0.5$  mg accuracy to measure the mass, and an environmental SEM (XL30 ESEM, FEI, Hillsboro, OR, USA) to inspect the microstructure of the material.

Reaction species present downstream of the plug were monitored by a residual gas analyzer (RGA) (SRS RGA 300, Stanford Research System, Inc., Sunnyvale, CA, USA) placed upstream of the vacuum pump with a variable leak valve to supply a controlled amount of gas to the mass spectrometer. For each new reactive gas, an initial oxidation survey was carried out for high temperatures with an initial plug of FF. An example spectrum for the analog RGA plot is shown in Fig. 2. Three recorded spectra are displayed: (1) a baseline spectrum (black) recorded right after evacuation of the flow tube to a base pressure below 13 Pa, showing no significant signal, (2) a spectrum (red) recorded during oxidation, showing products from the decomposition of FF and (3) a spectrum (blue) recorded at the end of the test, where the signal went back to the initial baseline. Data were collected in pressure-versus-time mode, monitoring up to ten species determined to be present during a survey experiment at a sampling rate of 0.5 or 1 Hz. For oxidation with  $O_2$ , the selected monitored species were  $H_2O$ ,  $N_2$ ,  $CO$ ,  $O_2$ ,  $Ar$ , and  $CO_2$ .

Separate calibration experiments were conducted in order to quantify gas species using the RGA. It was imperative that the RGA calibration was carried out at the same pressure and leak valve conditions used in the oxidation experiments. In these calibration experiments, the pure gases of interest formed during oxidation (e.g.,  $CO$ ,  $CO_2$ ) were introduced to the system at controlled mass flow rates while recording the pressure ( $P_2$ ) at the sampling port to the RGA. During the experiments, the leak valve was set to a fixed value on the micrometer, which resulted in pressures in the RGA systems in the range of  $1 \times 10^{-8}$  to  $4 \times 10^{-8}$  Torr. A calibration response for the RGA as a function of the downstream pressure was generated for each mass flow. The RGA response was observed to be linear with pressure and quadratic with mass flow.

## 2.2. Experimental protocol

We followed a strict protocol to characterize the test sample, insert it in the flow tube, and perform the experiment. First, the

length, radius, and mass of each FF plug were measured, and material densities were calculated. The sample was then inserted into the quartz tube as described above, and the system was evacuated to a base pressure  $P_s$  below 13 Pa. The gas bypass valves (BV1, BV2 and BV3) were opened to equilibrate the pressure up- and downstream of the sample and prevent movement of the FF plug upon introduction/extraction of flowing gases. The RGA system revealed outgassing of water from some of the FF samples during pump-down, likely due to atmospheric moisture trapped in the fibrous material [53]. The system was evacuated long enough for the RGA  $H_2O$  signal to zero, which ensured the oxidation measurements were unaffected by any water content. The system was then pressurized using neat argon gas at increasing flow rates from 4.5 to 36 mg/s to measure the permeability of the virgin sample at room temperature and verify the plug was defect-free. The permeability correlation for FF determined in [51] was used as a standard for quality-checking the sample insertion.

After permeability measurements, the system was heated to the target oxidation temperature. During the heating phase, which could take between 20 and 100 min, a constant Ar flow at 9 mg/s was supplied to the plug (bypass closed) to maintain an inert atmosphere and prevent any uncontrolled oxidation. The oxidation experiment was carried out at the target temperature by first evacuating the inert gas to a base pressure  $P_s < 13$  Pa. The mass flow controller for  $O_2$ ,  $CO_2$ , or  $CO$  was then activated. The oxidizing gas was flowed through the system for a target of 10 min at a constant rate while monitoring the absolute upstream pressure, differential pressure, and temperature. After a 10-min exposure, the oxidizing gas was evacuated to the base pressure  $P_s < 13$  Pa, the supply gas was switched back to a 9 mg/s flow of Ar, and the furnace was cooled.

The FF sample was removed once the temperature inside the furnace was less than 373 K by pushing from the backside of the plug, toward the pyrometer. This protected the exposed face from damage, keeping it intact for SEM inspection. The mass, length, and radius were again measured and compared to the initial state.

## 2.3. Uncertainty analysis

For fibrous insulators like FF, the largest uncertainty in experimental measurements using specimens of limited size is the variability of the material. A scatter of nearly 10% is found for the density of samples machined from the same material billet [51]. In addition, FF is known to have a non-negligible variability (e.g., compressed and expanded layers, variability of the TT direction) at large scale [51] that needs to be carefully considered when using the data for modeling large systems.

Experimental uncertainties in flow rate, pressure (absolute and differential), and temperature measurements were analyzed in a previous study [51], and were found to be  $\pm 7\%$ ,  $\pm 2\%$  and  $\pm 2\%$ , respectively. Uncertainties in the dimensioning and mass measurements were approximately  $\pm 1\%$ . However, a typical mass loss from the press-fit insertion and extraction of a plug into and out of the flow-tube setup was found to be  $\sim 35$  mg, or  $\pm 2\%$ . With these values and typical uncertainties on the gas viscosity of  $\pm 3\%$ , the overall uncertainty on the material intrinsic permeability and the permeability slip parameter (Section 3.1) were found to be  $\pm 10\%$  and  $\pm 2\%$ , respectively [51].

The uncertainty in the quantification of decomposition products is directly related to the uncertainty in the measured and calculated parameters which included sample mass  $m$ , flow rate  $\dot{m}$ , temperature  $T$ , pressure  $P_2$ , and RGA partial pressures  $p_i$  ( $\pm 3\%$ ). Based on these values, an overall root of the sum of the squares (RSS) uncertainty on the oxidation products of  $\pm 12\%$  was computed.

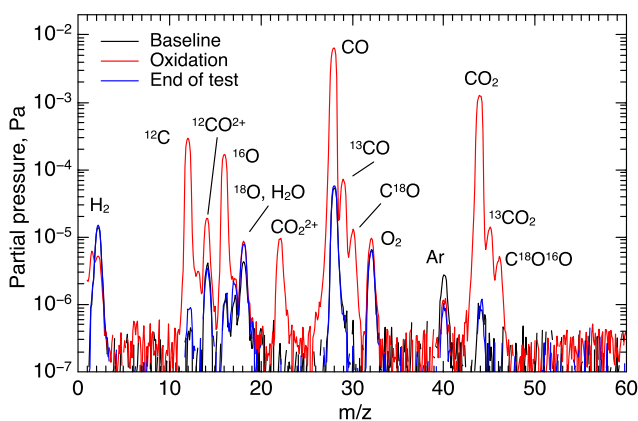


Fig. 2. Example of analog RGA spectra collected during an  $O_2$  oxidation experiment at 1373 K.

### 3. Experimental results and data analysis

#### 3.1. Permeability measurements

Measurements of the Klinkenberg permeability of FF were made at room temperature as well as at the temperature at which the samples were oxidized (highlighted in bold) (Table 1).  $K_0$  is the intrinsic permeability of the material and  $b$  is the Klinkenberg parameter that accounts for slip effects. The density of FF used in this study varied between 173 and 189 kg m<sup>-3</sup>, typical of the sample-to-sample variation of FF. All permeability measurements were obtained in Ar flow, and  $K_0$  and  $b$  were determined by a least-squares fit of measured quantities, as documented in [51,52,54]. A plot of the normalized permeability force  $F^\dagger$  as a function of the average pressure  $P_{avg}$  is shown in Fig. 3. The normalized permeability force is defined as:

$$F^\dagger = K_0(P_{avg} + b^*) \frac{\phi^\dagger}{\phi} \quad (1)$$

where

$$P_{avg} = (P_1 + P_2)/2 \quad (2)$$

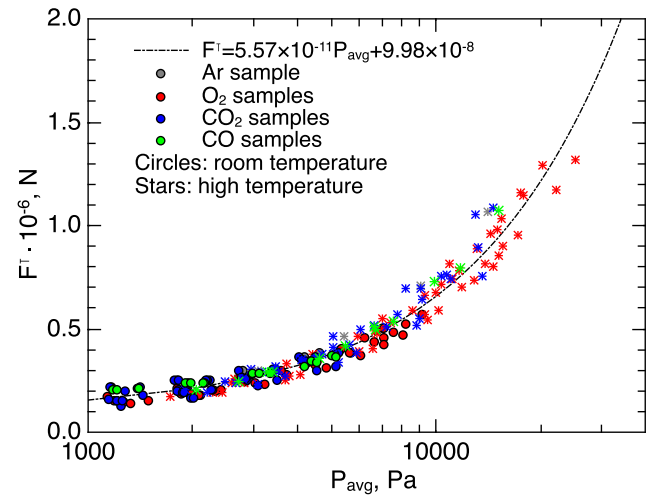


**Fig. 3.** All permeability data were measured in argon flow and scaled into a single curve that matches the permeability force versus the pressure fitting curve determined in [51]. Color labels identify samples tested under different gases after argon permeability measurements. Scatter of data is due to the variability of FF. (For interpretation of the references to colour in this figure legend, the reader is referred to the web version of this article.)

**Table 1**  
Summary of argon permeability measurements.

Sample	$\rho$ , kg/m <sup>3</sup>	T, K	$K_0$ , m <sup>2</sup>	$b$ , Pa
Ar	180	297	4.69E–11	4151
		<b>1505</b>	<b>6.93E–11</b>	<b>12,107</b>
O2_A	178	297	6.05E–11	1590
		<b>523</b>	<b>6.09E–11</b>	<b>2756</b>
O2_B	181	297	5.45E–11	1674
		<b>723</b>	<b>5.37E–11</b>	<b>4656</b>
O2_C	189	391	5.41E–11	2313
		<b>823</b>	<b>5.14E–11</b>	<b>5578</b>
O2_D	187	297	6.07E–11	1449
		<b>933</b>	<b>6.16E–11</b>	<b>5990</b>
O2_E	175	295	6.47E–11	1447
		<b>1082</b>	<b>6.72E–11</b>	<b>7491</b>
O2_F	182	361	6.24E–11	1989
		<b>1121</b>	<b>5.99E–11</b>	<b>8535</b>
O2_G	186	310	4.95E–11	1807
		<b>1319</b>	<b>5.06E–11</b>	<b>13,738</b>
O2_H	177	298	6.07E–11	2068
		<b>1507</b>	<b>5.99E–11</b>	<b>17,561</b>
CO2_A	175	297	6.45E–11	1576
		<b>684</b>	<b>6.57E–11</b>	<b>4348</b>
CO2_B	185	296	5.20E–11	1406
		<b>725</b>	<b>5.25E–11</b>	<b>5225</b>
CO2_C	176	296	6.43E–11	1373
		<b>985</b>	<b>6.56E–11</b>	<b>6621</b>
CO2_D	179	297	4.79E–11	3399
		<b>1035</b>	<b>6.02E–11</b>	<b>7427</b>
CO2_E	174	296	6.04E–11	1560
		<b>1185</b>	<b>6.32E–11</b>	<b>8839</b>
CO2_F	186	325	3.78E–11	4263
		<b>1226</b>	<b>4.96E–11</b>	<b>10,736</b>
CO2_G	178	297	4.46E–11	3997
		<b>1317</b>	<b>6.18E–11</b>	<b>9870</b>
CO2_H	173	296	5.09E–11	3765
		<b>1421</b>	<b>7.49E–11</b>	<b>10,105</b>
CO2_I	179	296	4.29E–11	4320
		<b>1514</b>	<b>6.85E–11</b>	<b>11,809</b>
CO_A	174	357	3.67E–11	6718
		<b>722</b>	<b>6.25E–11</b>	<b>4496</b>
CO_B	174	296	4.36E–11	4181
		<b>1127</b>	<b>6.16E–11</b>	<b>7864</b>
CO_C	180	296	3.88E–11	4656
		<b>1513</b>	<b>6.39E–11</b>	<b>11,617</b>



$$b^* = b \frac{\mu^*}{\mu} \sqrt{\frac{M T^*}{T M^*}} \quad (3)$$

$$\phi = 1 - \frac{\rho}{\rho_c} \quad (4)$$

and  $\rho_c = 1400 \text{ kg m}^{-3}$  and  $\phi^{\dagger} = 0.87$ . The term “normalized” here is used to indicate that the permeability force is scaled to the nominal FF porosity [51]. The plot shows that all data can be scaled to a single curve that conforms to the fitting determined during our previous work, for which values of  $K_0 = 5.57 \times 10^{-11} \text{ m}^2$  and  $b^* = 1792 \text{ Pa}$  were obtained [51]. The permeabilities data reported in Table 1 were all measured in the TT direction. IP values were measured by Marschall and Milos [52] for an old version of FF and by Panerai et al. [51] for the present version of the material.

### 3.2. Oxidation measurements

The conditions for this series of FF oxidation tests are listed in Table 2. The sample temperature  $T_s$  was slightly lower (2–8 K lower) than the temperature measured during the permeability measurements (cf. Table 1), due to the higher heat capacity of oxygen (compared to argon) to absorb thermal energy from the furnace resulting in a lower measured temperature. As shown in [51], the effect of temperature can be corrected by scaling the Klinkenberg coefficient of the permeability (cf. Eq. (3)). Similar to what observed in our previous work [55], for the high temperature experiments (at  $T_s > 1000 \text{ K}$ ) the pyrometer recorded a slight increase of less than 5 K in the sample surface temperature due to the exothermicity of the oxidation reaction. This was only observed for the  $\text{O}_2$  experiments.

The introduction of the oxidation gas as described above resulted in a transient rise in pressure (both absolute and differential) until steady-state conditions were reached. This rise lasted between 4 and 10% of the total oxidation time depending on the test conditions. Both values of the transient time  $t_{tr}$  and the total oxidation time  $t$  (from the start of exposure) are reported in Table 2. Preliminary numerical simulations of the experiments have highlighted the significance of the initial transient time  $t_{tr}$  in the modeling of the entire experiment [56].

The upstream ( $P_1$ ) and differential ( $\Delta P$ ) pressures were used during the experiment to monitor the oxidation of the FF sample.

The decomposition of the sample resulted in a decrease of the upstream pressure. The downstream ( $P_2$ ) pressure was computed as  $P_2 = P_1 - \Delta P$ . The upstream pressure  $P_1$  and differential pressure  $\Delta P$  listed in Table 2 are indicated by a subscript ‘0’ for the beginning of the steady-state phase, and by a subscript ‘e’ for pressure at the end of the test when the flow of the oxidizing gas was stopped. Experiments in Ar and CO, as well as experiments at low temperature in  $\text{O}_2$  (at  $T_s < 700 \text{ K}$ ) and in  $\text{CO}_2$  (at  $T_s < 1150 \text{ K}$ ) resulted in both  $P_1$  and  $\Delta P$  remaining nearly constant during the experiment. This indicated that no decomposition due to oxidation occurred within the sample. This observation was also corroborated by the RGA data. As a result, the material permeability remained constant. Conversely, at high temperatures (at  $T_s > 800 \text{ K}$  for the  $\text{O}_2$  tests and  $T_s > 1400 \text{ K}$  for  $\text{CO}_2$  tests), a constant drop in  $P_1$  and  $\Delta P$  suggested material decomposition due to oxidation, which might have an impact on the permeability. Note that a drop in  $P_1$  and  $\Delta P$  is further due to a shortening of the sample the experiments that exhibited material recession ( $\text{O}_2$  tests at  $T_s > 800 \text{ K}$ ). At intermediate temperatures, for both experiments in  $\text{O}_2$  and  $\text{CO}_2$ , a slight increase in  $P_1$  and  $\Delta P$  was observed, of the order of 50–100 Pa. This behavior was observed for temperatures close to the onset of oxidation (see samples  $\text{O}_2\text{-C}$  and  $\text{CO}_2\text{-E-F-G}$ , cf. Table 3) and was likely caused by a change in permeability, as further discussed in Section 3.4. An example of the three observed behaviors is also shown in Fig. 4 for experiments in  $\text{CO}_2$  flow.

Data from the oxidation of FF are summarized in Table 3, including sample temperature  $T_s$  and total oxidation time  $t$ , initial values for sample density ( $\rho_{s,0}$ ), mass ( $m_0$ ), length ( $L_0$ ) and diameter ( $d_0$ ), final values for sample density ( $\rho_{s,e}$ ), and diameter ( $d_e$ ), mass ( $\Delta m$ ) and recession ( $\Delta L$ ), and the total mass of CO ( $m_{\text{CO}}$ ) and  $\text{CO}_2$  ( $m_{\text{CO}_2}$ ) measured by mass spectroscopy, integrated over the entire total oxidation time. High-temperature argon exposure resulted in a mass loss,  $\Delta m$ , of 0.033 g, which was equivalent to the mass loss measured when a sample was inserted and immediately removed from the flow tube (between 0.02 and 0.04 g). This validated the use of argon as the conditioning gas to set the flow, temperature, and pressure for all the experiments.

The mass loss,  $\Delta m$ , and recession,  $\Delta L$ , of the plug increased for the  $\text{O}_2$  and  $\text{CO}_2$  experiments with increasing temperature, while the CO exposure showed insignificant changes in mass. Changes in FF density, computed from the value of Table 3, showed a small

**Table 2**  
Summary of test condition during oxidation of FiberForm.

Sample	Gas	$\dot{m}$ , g s <sup>-1</sup>	$T_s$ , K	$t$ , s	$t_{tr}$ , s	$P_{1,0}$ , Pa	$\Delta P_0$ , Pa	$P_{1,e}$ , Pa	$\Delta P_e$ , Pa
Ar	Ar	2.36E–03	1503	605	24	10,606	10,383	10,580	10,344
O2_A	O <sub>2</sub>	2.36E–03	518	600	21	2172	2102	2160	2070
O2_B	O <sub>2</sub>	2.39E–03	718	600	30	2922	2833	2948	2857
O2_C	O <sub>2</sub>	2.34E–03	818	604	65	3546	3470	2608	2513
O2_D	O <sub>2</sub>	2.34E–03	928	595	42	3673	3583	2468	2373
O2_E	O <sub>2</sub>	2.34E–03	1085	605	47	3668	3537	2513	2380
O2_F	O <sub>2</sub>	2.36E–03	1116	631	58	4079	4002	2518	2420
O2_G	O <sub>2</sub>	2.34E–03	1314	602	63	5325	5211	3173	3046
O2_H	O <sub>2</sub>	2.34E–03	1502	602	53	6180	6060	1771	1618
CO2_A	CO <sub>2</sub>	2.27E–03	683	605	35	2065	1962	2065	1982
CO2_B	CO <sub>2</sub>	2.29E–03	721	602	43	2408	2299	2398	2287
CO2_C	CO <sub>2</sub>	2.31E–03	983	602	44	2674	2555	2646	2502
CO2_D	CO <sub>2</sub>	2.27E–03	1031	605	41	2847	2763	2836	2728
CO2_E	CO <sub>2</sub>	2.29E–03	1182	606	54	3001	2887	3055	2929
CO2_F	CO <sub>2</sub>	2.29E–03	1221	663	48	3374	3290	3592	3478
CO2_G	CO <sub>2</sub>	2.29E–03	1314	605	82	3880	3625	4013	3724
CO2_H	CO <sub>2</sub>	2.31E–03	1413	605	58	4176	4057	3862	3715
CO2_I	CO <sub>2</sub>	2.29E–03	1508	601	65	5325	4892	4654	4220
CO_A	CO	2.08E–03	719	602	25	2462	2365	2450	2349
CO_B	CO	2.04E–03	1121	601	34	3267	3160	3273	3153
CO_C	CO	2.06E–03	1508	603	34	3954	3846	3968	3820

**Table 3**

Summary of FiberForm oxidation measurements.

Sample	$T_s$ , K	$t$ , s	$\rho_{s,0}$ , kg/m <sup>3</sup>	$m_0$ , g	$L_0$ , mm	$d_0$ , mm	$\rho_{s,e}$ , kg/m <sup>3</sup>	$\Delta m$ , g	$\Delta L$ , mm	$d_e$ , mm	$m_{CO_2}$ , g	$m_{CO}$ , g
Ar	1503	605	180	1.367	20.07	21.98	182	0.033	0.01	21.54	–	–
O2_A	518	600	178	1.366	20.12	22.06	183	0.033	0.06	21.50	0.000	0.000
O2_B	718	600	181	1.442	20.88	22.03	183	0.044	0.01	21.59	0.003	0.000
O2_C	818	604	189	1.439	19.88	22.07	174	0.545	5.77	21.54	0.463	0.016
O2_D	928	595	187	1.425	20.10	21.96	171	0.623	7.20	21.54	0.499	0.025
O2_E	1086	605	175	1.357	20.20	22.11	162	0.691	7.72	21.77	0.404	–0.001
O2_F	1116	631	182	1.397	20.07	22.05	170	0.687	8.63	21.54	0.418	0.081
O2_G	1314	602	186	1.430	20.09	22.06	168	0.790	9.69	21.59	0.216	0.330
O2_H	1502	602	177	1.372	20.08	22.14	127	1.041	12.90	21.49	0.012	0.895
CO2_A	683	605	175	1.357	20.16	22.10	177	0.016	0.00	21.87	–	0.002
CO2_B	721	602	185	1.404	20.10	21.95	190	0.018	0.04	21.54	–	–0.003
CO2_C	983	602	176	1.350	20.14	22.04	177	0.022	0.01	21.75	–	0.001
CO2_D	1031	605	179	1.393	20.49	22.02	185	0.025	0.12	21.53	–	0.001
CO2_E	1182	606	174	1.357	20.16	22.10	178	0.024	0.04	21.79	–	0.002
CO2_F	1221	663	186	1.437	20.02	22.17	189	0.063	0.03	21.52	–	0.023
CO2_G	1314	605	178	1.386	20.50	22.00	163	0.170	0.01	21.54	–	0.201
CO2_H	1413	605	173	1.330	20.08	22.05	139	0.316	0.02	21.54	–	0.274
CO2_I	1508	601	179	1.360	20.02	22.01	134	0.386	0.02	21.50	–	0.377
CO_A	719	602	174	1.321	20.08	21.94	178	0.021	0.02	21.52	–	–
CO_B	1121	601	174	1.331	20.12	22.01	180	0.020	0.04	21.50	–	–
CO_C	1508	603	180	1.383	20.12	22.06	184	0.036	0.03	21.55	–	–

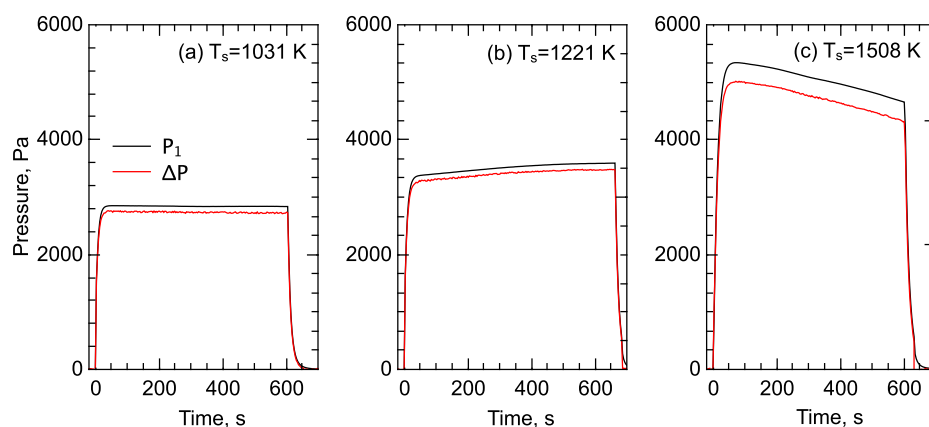


**Fig. 4.** The upstream pressure,  $P_1$ , and differential pressure,  $\Delta P$ , across the sample, exhibit qualitative differences over a narrow temperature range during oxidation experiments in  $CO_2$ . The temperature for oxidation increases from the left panel to the right panel. (a)  $CO_2$  oxidation at  $T_s = 1031$  K (CO2\_D), (b)  $CO_2$  oxidation at  $T_s = 1221$  K (CO2\_F), (c)  $CO_2$  oxidation at  $T_s = 1508$  K (CO2\_I).

increase (<3%) in material density for tests in which negligible mass loss was measured. This is likely due to compression of the sample during the press-fitting insertion. For completeness we have reported variations in the sample diameter measured prior to insertion ( $d_0$ ) and after removal ( $d_e$ ). For experiments in which oxidation occurred, the density of the sample decreased as a result of mass loss and recession. The reported data are as measured and are not corrected for the press-fitting density increase. Significant recession was measured for experiments in oxygen. However, the sample length remained constant for  $CO_x$  species. Based on mass loss and recession measurements, and on the Thiele number analysis approach described in [47], FF samples tested in  $CO_2$  and in low temperature  $O_2$  ( $T_s \lesssim 1000$  K) exhibited volumetric oxidation and were determined to be in a pure reaction-limited regime. High temperature  $O_2$  experiments approached instead the diffusion-limited regime. Future efforts will be dedicated at developing an accurate method to quantify the extent of the oxidation zone and in-depth gradients of porosity, density and permeability for specimens that exhibited volumetric decomposition.

Fig. 5 shows an example of the FF (O2\_H) following a 10-min exposure to oxygen gas at 1502 K compared to a virgin sample at

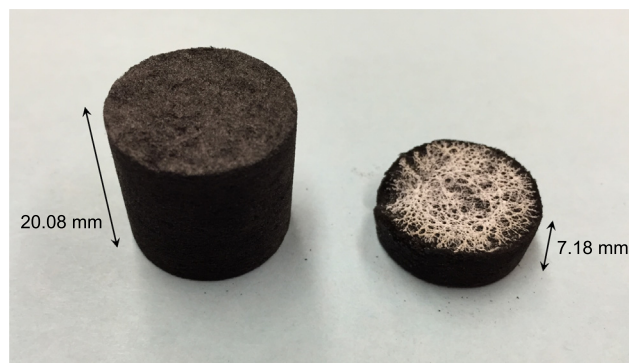


**Fig. 5.** FiberForm sample before (left) and after oxidation (right) in  $O_2$  at 1502 K (O2\_H).

the left. Here, significant macroscopic recession was observed, with more than half of the initial volume consumed. The formation of a whitish residue was observed at the surface, similar to observations made during past flow-tube oxidation experiments on FF in

air gas [47]. We attribute this to the presence of calcium-rich impurities found in FF, as reported in past investigations on the material [47]. SEM analysis of FF samples after oxidation suggests that Ca impurities are contained in the lumen of FF fibers and get released during oxidation as a fiber decomposes and the lumen opens up. The release of Ca might speed up oxidation kinetics. Further work should be done to investigate this phenomenon in detail.

Real-time mass spectral data was collected for specific ion peaks corresponding to molecules resulting from the oxidation of FF. An example trace for  $O_2$  and  $CO_2$  oxidation that highlights the product partial pressures versus time ( $p_i$  vs.  $t$ ) is shown in Fig. 6. The RGA was configured to monitor the main compounds identified in Fig. 2, which included  $O_2$  ( $m/z=16$ ),  $H_2O$  ( $m/z=18$ ),  $CO/N_2$  ( $m/z=28$ ),  $Ar$  ( $m/z=40$ ), and  $CO_2$  ( $m/z=44$ ). The RGA system has a mass resolution ( $m/\Delta m$ ) of 800 which was insufficient to resolve the  $CO$  and  $N_2$  peaks. For the present set of experiments, this was not a concern due to the verified high purity of  $O_2$  and the extensive leak testing. In addition, the detection of  $CO$  over  $N_2$  was further corroborated by tracking the increase in the  $m/z=12$  to  $m/z=14$  ratio. For all experiments, upon the introduction of the oxidizer, there was a clear increase of  $CO$  and  $CO_2$  at the start of oxidation ( $t=0$ ) that persisted until the oxygen was shut off, approximately 600 s later. From here, the  $CO_x$  species returned to system baseline. For  $O_2$  depicted in Fig. 6(a), at no point was there an increase in oxygen, which indicated a tight press-fit seal and no leakage of oxygen around the FF plug. Likewise, the argon and water partial pressures did not change meaningfully in these measurements. For  $CO_2$ , as can be seen in Fig. 6(b), only increases in C- and O-related species were observed.

Fig. 7 shows the pressure dependence (left panels) and corresponding RGA partial pressures (right panels) during  $O_2$  oxidation. The small, initial decrease in both pressure and RGA signal is due to the manual adjustment of the mass flow rate to the desired value. The progression from low temperature (top panels) to high temperature (bottom panels) depicts the observed pressure gradient as the material is oxidized, and suggests three major mechanisms. At “low” temperature, the  $O_2$  passes through the sample, resulting in no mass loss and no formation of  $CO_x$ . At moderate temperatures in the middle panel, a small pressure loss is observed, with a more rapid mass loss, and the prominent formation of  $CO_2$ . At the highest temperatures, the mass loss occurs rapidly and the  $CO_x$  species is almost entirely  $CO$ . Only a minimal amount of  $CO_2$  was observed in the second half of the high-temperature experiment ( $t > 250$  s). This  $CO_2$  signal increased over time in conjunction with a drop in the  $CO$  signal. This observation is further discussed in Section 4.

Fig. 8 compares low temperature  $CO_2$  (Fig. 8(a), 983 K) with high-temperature  $CO_2$  (Fig. 8(b), 1413 K) in a similar manner.  $CO_2$  observations are qualitatively similar to that reported for oxygen. At low temperature, there was nearly no decomposition (flat  $P_1$  and  $\Delta P$ ) and the oxidizer ( $CO_2$  in this case) went through the porous medium. At high temperature, significant formation of  $CO$  was observed. For all  $CO$  tests (Fig. 9), only  $CO$  was detected by the RGA and there was no mass loss. This suggests that  $CO$  simply permeated the FiberForm plug, without net yield of  $CO$ .

### 3.3. Quantification of oxidation products

Quantification of the oxidation products required careful measurement of the mass flow, the downstream pressure, and the RGA partial pressure response for gases of interest. For experiments with  $CO_2$  and  $CO$ , these measurements were a straightforward calibration measurement as described above. Experiments in  $O_2$ , where  $CO$  and  $CO_2$  products were concurrently detected (e.g., right panel of Figs. 7(b) and 8(b)), required more involved measurements. In the presence of  $CO_2$ , the  $CO$  fragment ( $m/z=28$ ) is a linear combination of  $CO^+$  formed in the  $CO_2$  ionization process and direct  $CO$  ionization. From the  $CO_2$  calibration measurements, the  $CO^+$  contribution from fragmentation was 9%. This agrees with the literature value of 9.8% [57]. We corrected the  $m/z=28$  contribution from  $CO_2$  fragmentation using the relation  $CO^+ = S_{28} - 0.09S_{44}$  where  $S_n$  is the  $p_i(t)$  signal for the assigned mass. Signals were also baselined to the  $S_n$  signal in the presence of only argon. The resulting  $p_i(t)$  was then integrated to yield the amount of  $CO_x$  generated. The carbon content of each species calculated in this manner were summed to calculate the amount of carbon consumed at each temperature.

In each of the measurements for  $O_2$ , the calculated amount of carbon lost was compared to the balance-measured loss reported in Table 3. The comparison is shown in Fig. 10(a) as a function of oxidation temperature  $T_s$ . The left axis shows the carbon contained in the gas phase  $CO_2$  (black dots) and  $CO$  (gray dots). The right axis reports the carbon loss from the material. Here, we compare FF carbon converted into sum-total gas phase carbon represented as blue dots with the mass loss measured by an external balance (blue squares). Consistent with the previous figures, no measurable mass loss was observed for temperatures  $< 700$  K. This also showed no  $CO$  or  $CO_2$  formation. Fig. 10 also illustrates the trend of increasing  $CO/CO_2$  ratio with increasing temperature in the  $O_2$  oxidation experiments. At 823–1100 K, the reaction product is dominated

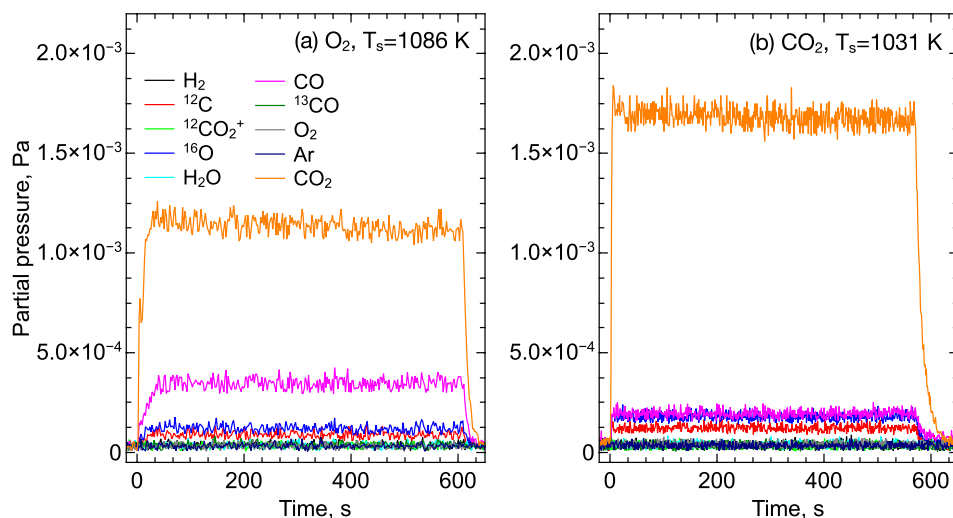
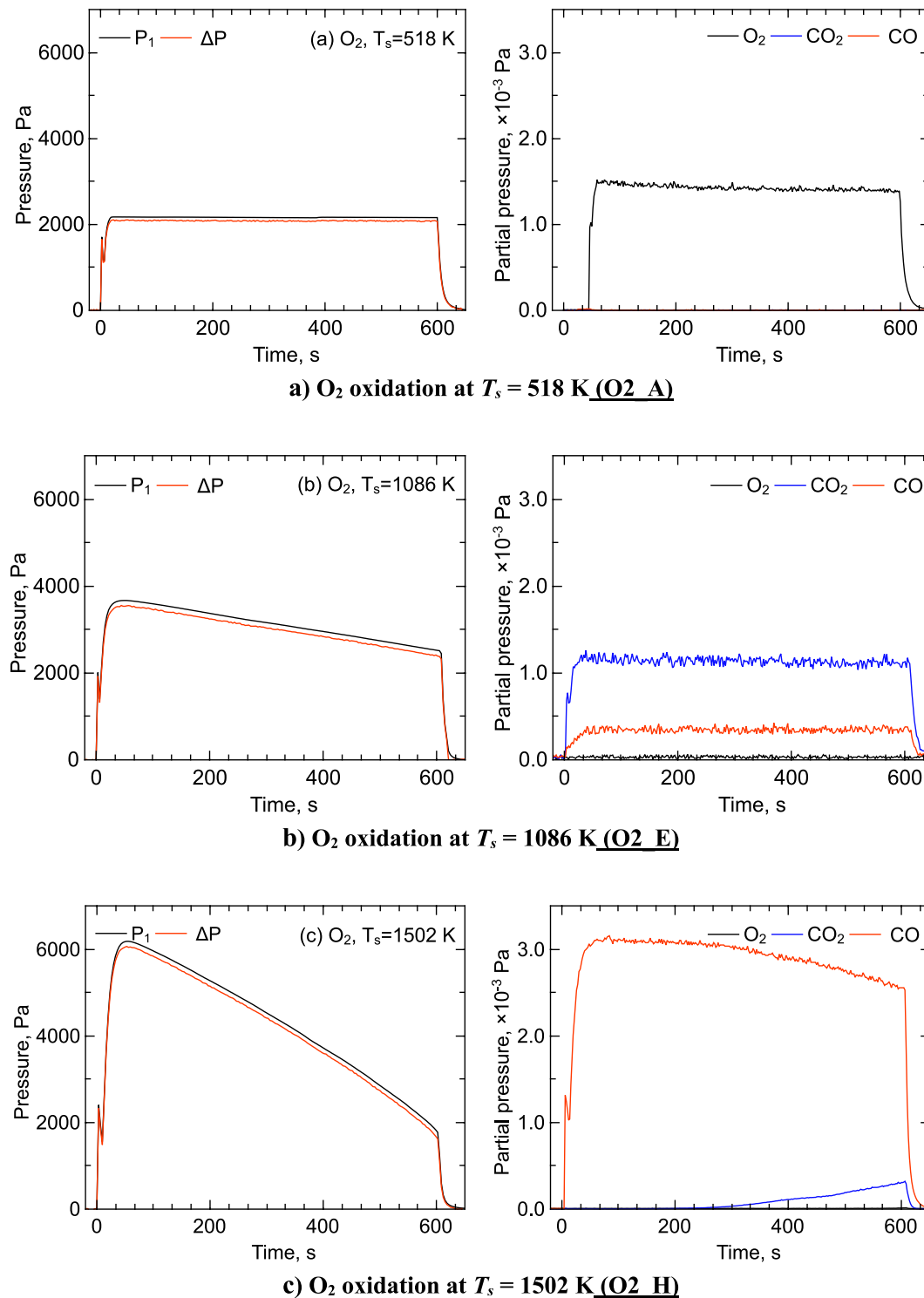


Fig. 6. Examples of RGA  $p_i$  vs.  $t$  traces for (a)  $O_2$  oxidation at 1086 K (O2\_E) and (b)  $CO_2$  oxidation at 1031 K (CO2\_D).





**Fig. 7.** Left: pressures as a function of time for the oxidation of FiberForm by O<sub>2</sub> at increasing temperature. Right: RGA  $p_i$  response as a function of time.

by CO<sub>2</sub>; however, above 1200 K, it is dominated by CO. The CO/CO<sub>2</sub> ratio of 1 occurs at  $\sim 1260$  K. Discrepancies between the weighed carbon loss and that calculated by mass spectrometry are discussed in the following section.

The CO<sub>2</sub> oxidation shows very similar results in Fig. 10(b). Here, the low temperature is dominated by the CO<sub>2</sub> signal, which passed unreacted through the FF plug. Above 1200 K, the CO signal began to increase, with a rapid decrease in the CO<sub>2</sub> signal. The measured weight loss here agrees well with the computed carbon loss. A plot

for CO is omitted; as shown in Table 3, the CO flow experiments exhibit no change in CO content at any experimental condition.

### 3.4. Surface microscale imaging

Micro-scale imaging was performed to investigate changes in the material structure due to oxidation. Below 700 K, no oxidation occurred and FF remained in its virgin state. Scanning electron micrographs of the sample front surface are presented in Fig. 11

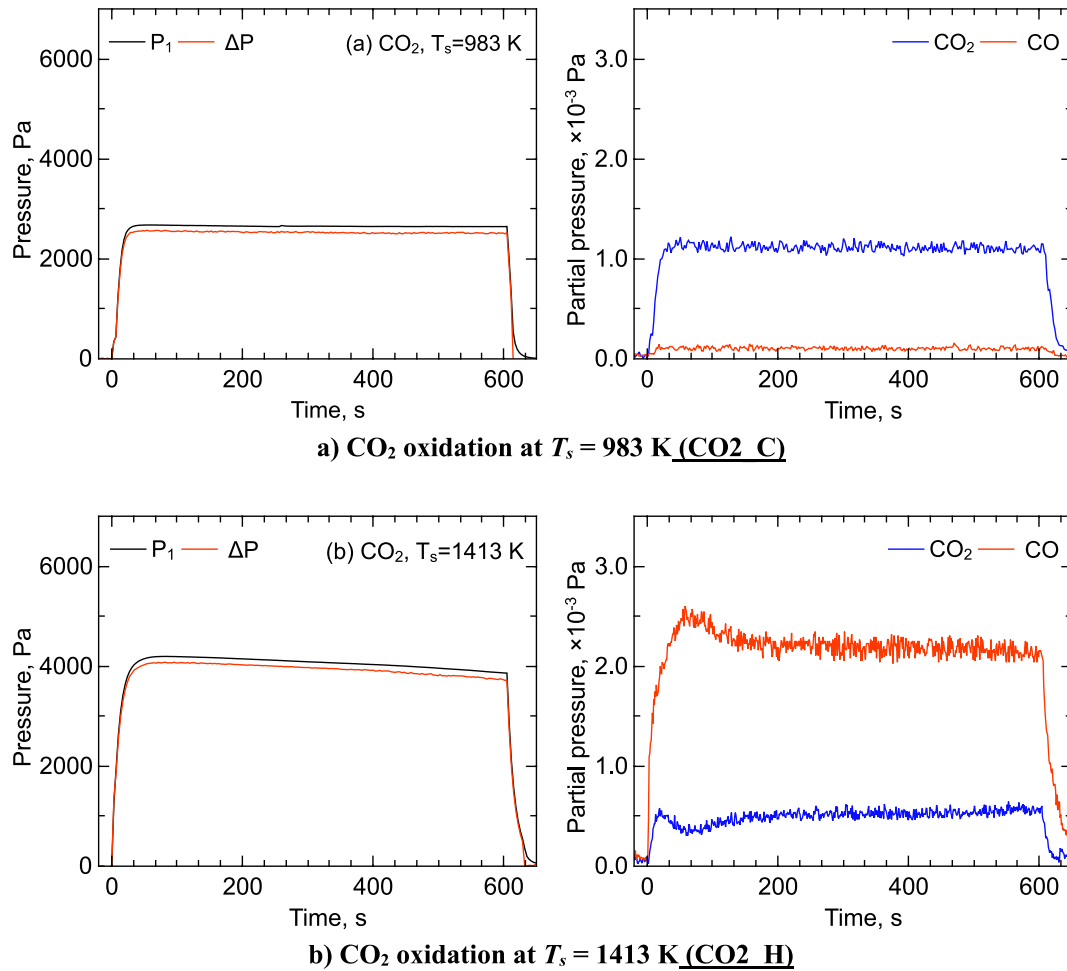


**Fig. 8.** Left: pressures as a function of time for the oxidation of FiberForm by CO<sub>2</sub> at increasing temperature. Right: RGA  $p_i$  response as a function of time.

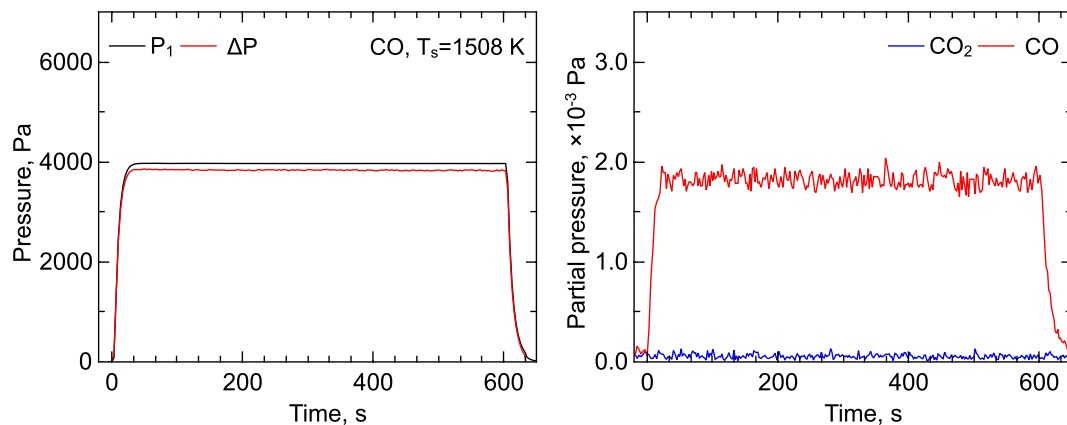


**Fig. 9.** Left: pressures as a function of time for the oxidation of FiberForm by CO at 1508 K (CO\_C). Right: RGA  $p_i$  response as a function of time.

at two magnifications. They show the typical fibrous structure of FF, made of  $\approx 1.6$ -mm long,  $\approx 11$ - $\mu$ m diameter fibers organized in clusters (red arrows) and bundles (orange arrows). The higher-resolution picture (Fig. 11b) shows the typical lobular cross-section of the rayon-derived fibers that composed the current version of FF. The fibers are bonded together by a resin binder carbonized during manufacturing. Residuals of this binder can be seen in the virgin material (yellow arrows) at the intersection of fibers and at the location of fibers' clumps (red and orange arrows).

The high-temperature oxidation results in very different SEM images. Fig. 12 shows SEM images of FF oxidized by O<sub>2</sub> (Fig. 12 (a, b), sample O2\_H, 1502 K) and CO<sub>2</sub> (Fig. 12 (c, d), sample CO2\_I, 1508 K), respectively. For the FF tested in oxygen, the micrographs revealed a substantial narrowing of the carbon fibers, similar to what was observed in previous studies on the oxidation of FF in air [47]. On closer inspection, the fibers had a large number of pits on their surface compared to virgin FF [47]. As fiber thinning and pits would further increase FF porosity, the permeability in

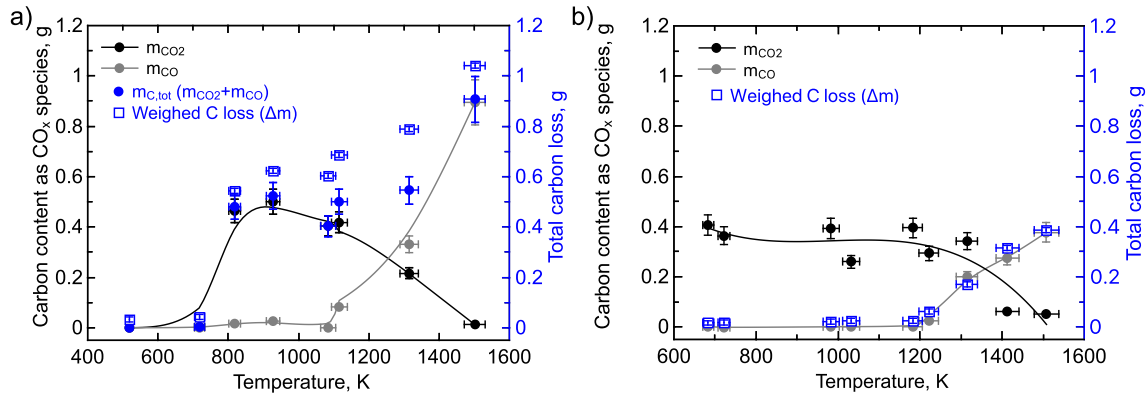


Fig. 10. Mass loss and mass of carbon produced by  $\text{CO}_x$  species for (a)  $\text{O}_2$ , (b)  $\text{CO}_2$ .

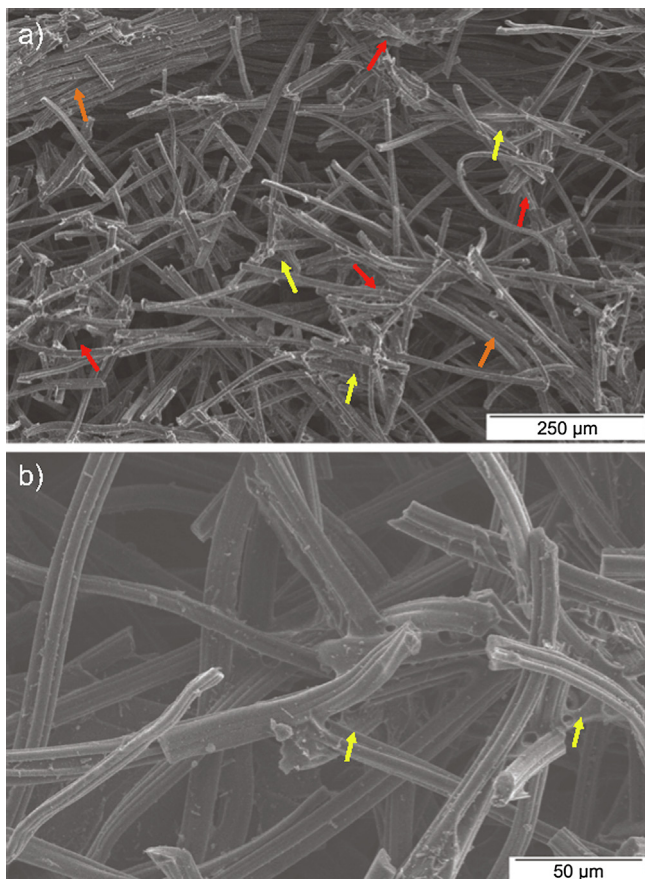


Fig. 11. SEM images of the front surface of FF tested at  $T < 700$  K.

this reacted zone would also be affected. The thinning of the fibers could potentially increase the permeability by allowing the gas to flow more freely. Pitting, however, could increase surface area via surface roughening, thus increasing the “drag” imposed by the fiber on the flow. This would therefore result in a decrease in permeability. In addition, it is noted that pitting would affect the effective reactivity of the fibers by increasing the surface area available for reactions to occurs [36].

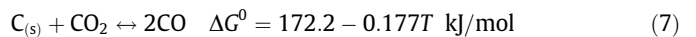
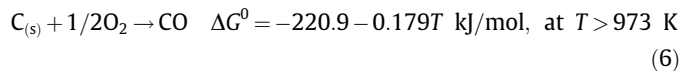
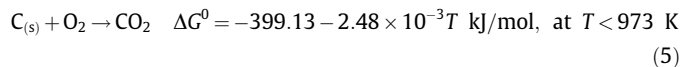
A further interesting observation from the SEM images is the absence of the charred binder in the oxidized FF. No traces of it were found in the samples tested at the highest temperatures. This suggests the carbonized binder has a higher reactivity than the fibers and decomposes faster during oxidation [58]. The decompo-

sition of the binder, in addition to the thinning of the fibers, results in a loss of rigidity and mechanical strength for the oxidized material. Indeed, while the samples preserved their shape after testing, the material was substantially softened in the oxidized region and crumbled upon application of a very light load. The weakening of the material is considered to be one of the main factors determining spallation (mechanical erosion) during FF exposure to high-shear flows [59]. In the present experiments, a contribution of mechanical erosion might explain the discrepancies observed in Fig. 10 between the carbon loss measured by weighing the samples and those obtained from mass spectrometry.

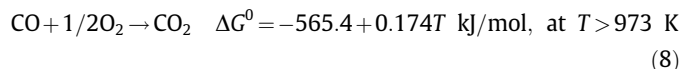
#### 4. Discussion

The decomposition of the carbon fibers in the FF material has previously been shown to be an in-depth phenomenon [17]. At the harshest condition of atmospheric entry (typically surface material temperatures above 2000 K), oxidation of the fibrous preform and the carbonized matrix would result in a rapid recession of the macroscopic surface exposed to the gas flow, with little penetration of the boundary layer reactants into the porous material. Under such conditions, ablation is a diffusion-limited process and the oxidizers would mostly react within the forward  $\approx 500$   $\mu\text{m}$  of the material. The temperatures investigated in this study, occurring at milder entry conditions, are characteristic of a reaction-limited regime. In this instance, the oxygen from the incoming flow permeates the fibrous structure and oxidizes from within [17]. The FF at the present flow tube conditions has a low-to-moderate Thiele number ( $\Phi < 1$ ) [12,47], thus we expect physical decomposition processes to occur at volume depths larger than a millimeter.

The oxidation of carbon can be summarized with the following heterogeneous global reactions:



and this homogeneous global reaction:



The first reaction requires surface dissociation of  $\text{O}_2$  on the carbon substrate to form  $\text{CO}_{ad}$ , followed by oxidation by an additional O-atom (either in an Eley-Rideal or a Langmuir-Hinshelwood

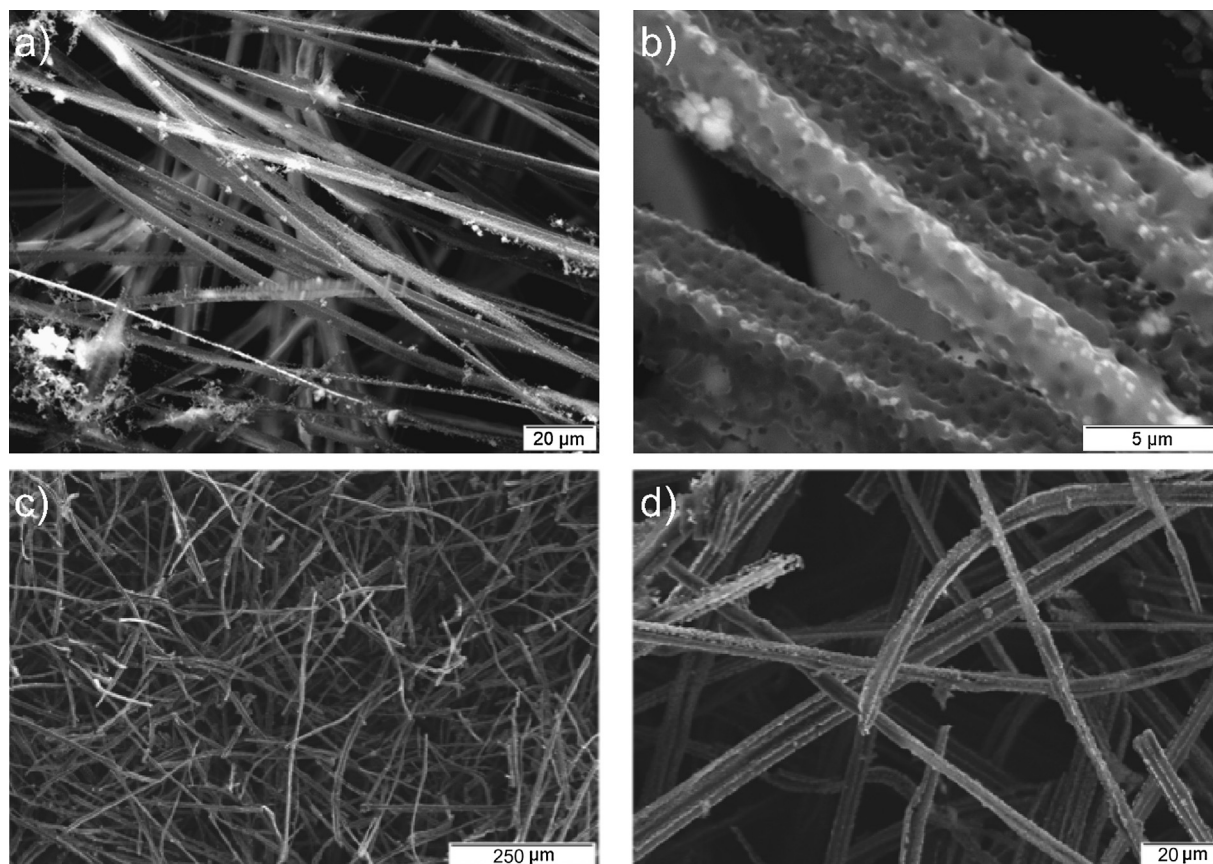


Fig. 12. SEM images of the front surface of oxidized FiberForm tested in  $O_2$  (a, b) and  $CO_2$  (c, d) at 1500 K.

mechanism) [60,61]. Studies have shown that both carbon dioxide and carbon monoxide are primary products of the oxidation of carbon [39,62]. Both can be directly produced by the desorption of carbon-oxygen complexes, without the need of Eqs. (7) and (8) to occur. The Gibbs-free energy for carbon-oxidation at standard pressure favors formation of  $CO_2$  at temperatures below 973 K, while above 973 K CO formation becomes more thermodynamically favored (see Eqs. (5) and (6)). Eq. (7) describes the well-known Boudouard equilibrium (BE) and becomes a viable process in the presence of excess  $CO_2$ , favored at lower temperatures when considering the Ellingham diagram for the listed reactions [47].

As expected, the results in Fig. 10 qualitatively agree with the carbon gasification results because our experiments utilize the same reaction scheme [39,63]. However, our observations show the CO/ $CO_2$  equilibrium point for both  $O_2$  and  $CO_2$  oxidation occurs between 1250 and 1350 K, which is significantly higher than the BE value of 973 K. The discrepancy suggests that, in the experiments, the oxidation process was not in equilibrium.

We now consider  $CO_2$  formation at the higher temperatures. Results in Fig. 7(c) ( $O_2$ -H, 1502 K oxidation in  $O_2$ ) showed a significant increase in  $CO_2$  production after 250 s of  $O_2$  oxidation with a corresponding decrease in CO. This observation has ramifications for proper treatment of gasification reactions as the surface dynamics may not be captured by bulk gas flow models with the assumption of equilibrium of CO and  $CO_2$  alone. Table 3 reports a loss of 12.9 mm in 10 min, a 1.29 mm/min recession rate, assuming the process is linear. At the time  $CO_2$  production was observed (4.2 min after exposure started), a 5.4 mm recession can be estimated, which is 25% of the original plug length. A simplified schematic of the reaction leading to  $CO_2$  at these high temperatures is shown in Fig. 13. As  $O_2$  flows towards and through the FF sample, it

reacts with the front face and the first few millimeters of the material, producing primarily CO (Eq. (6)) and a small fraction of  $CO_2$  (Eq. (5)). This region is labelled as “reaction zone 1” in Fig. 13. The products formed in this zone were transported through the sample and interacted with the back material in the region labelled as “reaction zone 2”. As inferred from the CO experiment, CO permeated through sample without reacting with the carbon.  $CO_2$ , however, oxidized the material via Eq. (7), which was out of equilibrium due to the lack of CO on the surface. From here, excess CO was formed, as shown in Table 3 for sample  $CO_2$ \_I (1508 K). As oxidation got underway, “reaction zone 2” was long enough for all  $CO_2$  to be converted in CO. Rapid recession at the higher temperatures shortened the length of “reaction zone 2”, which allowed unconverted  $CO_2$  to escape the plug without further reduction.

The suggested mechanism was further studied in a subsequent experiment that doubled the length of the FF plug shown in Fig. 14. This showed no increase in  $CO_2$  over the 600-s oxidation at similar conditions to the shorter plug, and resulted in mass losses within 1.2% and recession within 0.5% reported for the shorter plug. This suggests that a longer “reaction zone 2” allows for all the  $CO_2$  produced in “reaction zone 1” to be reacted. Note that the experiment with the double plug was intentionally started with the an open bypass to ease pressure accommodation at the beginning of the test. This produced the increase in  $O_2$  and  $CO_2$  observed in Fig. 14b for  $t < 0$ . Such feature is negligible and not relevant to the discussed observations.

The results from the  $CO_2$  experiments that showed no detectable recession and significant mass loss indicated a lower FF reactivity to  $CO_2$  than  $O_2$ , and in-depth decomposition through the FF material even at temperature as high 1500 K. At those conditions, the decomposition mechanism is mainly characterized by the



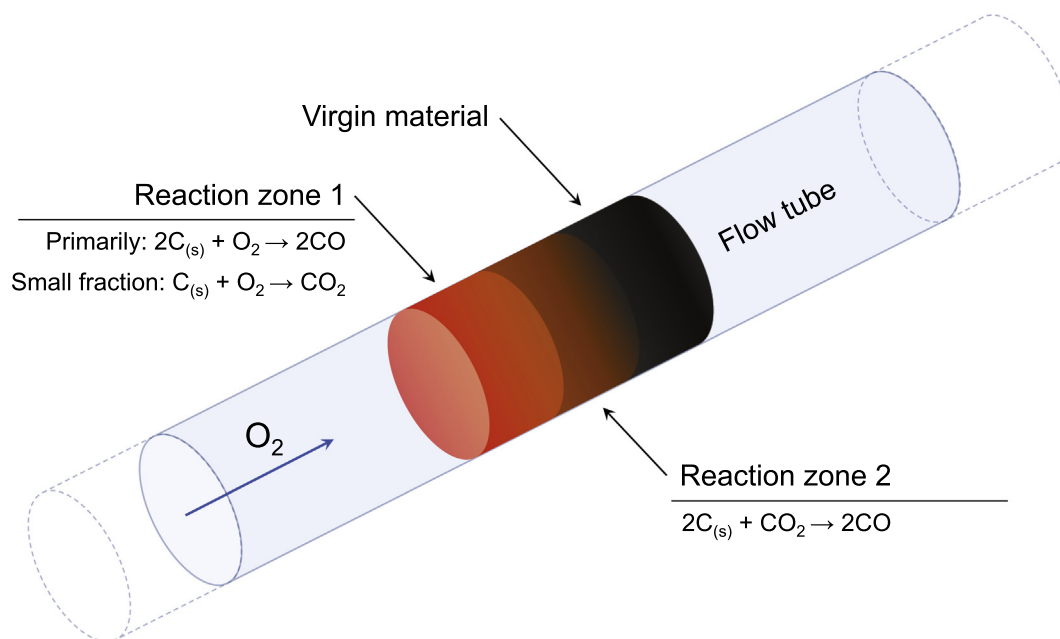


Fig. 13. Schematic of the mechanism of the high-temperature oxidation of FiberForm exposed to a constant flow of  $O_2$ .

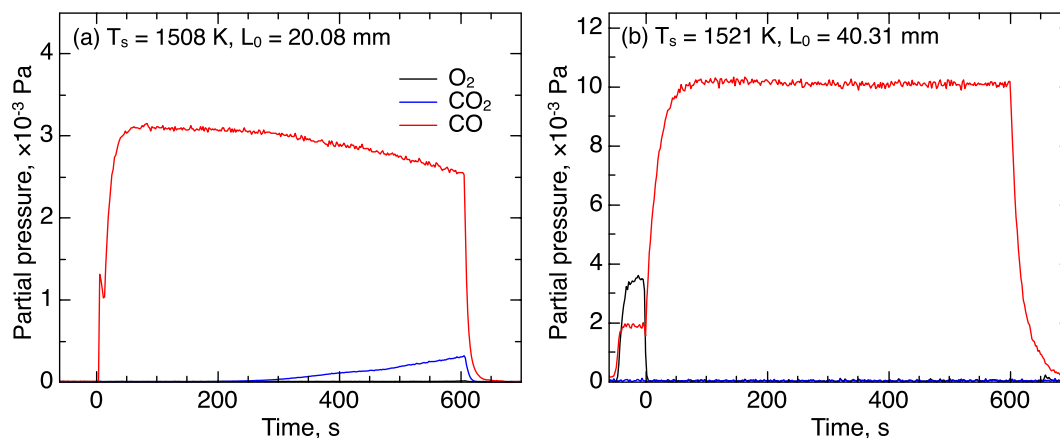


Fig. 14. Comparison of RGA signal at  $\sim 1500 \text{ K}$  for  $O_2$  oxidation for plug lengths of 20 mm and 40 mm.

Boudouard reaction (only “reaction zone 2”) and the produced CO that does not react with the hot porous char.

The adsorption of reactants onto the surface of the carbon fibers may further affect the desorption of CO at different temperatures, resulting in the variation expected from the BE. To consider a possible mechanism, we turn to studies of CO and  $CO_2$  exposure of graphite that investigated the temperature-programmed desorption (TPD) of CO following adsorption at room temperature, and at temperatures greater than 800 K [64]. For room temperature adsorption, CO TPD peaks occurred at 393, 503, and 673 K. For CO adsorbed at temperatures exceeding 800 K, the TPD peaks shifted to 973 and 1093 K. This was explained by citing two different CO surface species. The lower temperature TPD peaks cited intact carbonyl or ether groups adsorbed onto the carbon surface. These have low activation energies to desorption ( $E_a = 105\text{--}184 \text{ kJ mol}^{-1}$ ). The higher temperature species are more tightly bound to the carbon; in fact, Marchon et al. [60] suggested the oxygen forms a double bond with a surface carbon, forming a semiquinone, which requires the breaking of two C–C bonds to free the CO species with a much higher desorption activation energy

( $E_a = 268\text{--}347 \text{ kJ mol}^{-1}$ ). This high-temperature feature was also observed in  $O_2$ ,  $H_2O$ , and  $CO_2$  adsorption experiments [60]. Szymański et al. [65] also supported this analysis. Their Table 2 highlights the desorption temperatures of differently sourced CO. For lower temperatures (870–930 K), the CO release is often seen from phenolics and hydroquinonic groups. Carbonylic and quinonic bonds are prevalent at 1070–1253 K [65,66], which is partially in the range observed in our work. This brief analysis suggests that discrepancies between our results and the BE may also lie in different adsorption sites on the porous material.

## 5. Conclusion

The presented work explores the oxidation of carbon-based materials in forced-flow conditions using the simplest oxidizing gases:  $O_2$ , CO, and  $CO_2$ . The FF material was exposed at temperatures and flow conditions expected for mild atmospheric entry conditions to both Earth and Mars. The oxidation from  $O_2$  undergoes a dissociation process to form a mixture of CO and  $CO_2$  with the ratio governed primarily by the Boudouard reaction. As



recession proceeds deep into the carbon material, the reaction kinetics drive the changes observed from primarily CO to a mixture of CO and CO<sub>2</sub>. Unsurprisingly, temperature governs the ratio of product species, CO and CO<sub>2</sub>, through the Boudouard reaction.

Mass spectrometry results quantified the yield of CO<sub>x</sub> following oxidation from O<sub>2</sub>, CO<sub>2</sub>, and CO. The correlation to overall mass loss was reasonable for O<sub>2</sub> and very good for CO<sub>2</sub> exposures. For high temperatures, the O<sub>2</sub> flow was converted into a mixture of CO and CO<sub>2</sub>, while the CO<sub>2</sub> converted only to CO. Evidence from low temperature CO and CO<sub>2</sub> experiments does not indicate any gas-phase reactions, or gas interaction with dangling O-atoms on the wall of the quartz tube. Thus, the gas-surface reactions of the oxidation gas and the carbon fibers are thought to dominate over gas-gas reactions in the production of oxidation products.

Fiber thinning and pitting was observed following O<sub>2</sub> oxidation along with significant recession. Pitting alone was observed following oxidation with CO<sub>2</sub> with negligible recession but noticeable mass loss.

The results presented here can be used by the ablation community to construct and calibrate models that incorporate the chemical interaction of reactive gas species with the FF backbone of lightweight carbon/phenolic ablators. Using the procedures presented here will benefit future experiments of phenolic-based ablators built with the FF backbone, and novel materials such as carbon weaves and those coupling silicone sealants with phenolic materials.

## Conflict of interest

None declared.

## Acknowledgments

This work was supported by an award (NNX14A197G) under an Early Stage Innovation grant from NASA's Space Technology Research Grants Program. We acknowledge the contribution and insight of Jochen Marshall in the realization of the experiments.

## References

- [1] R.I. Baxter, R.D. Rawlings, N. Iwashita, Y. Sawada, Effect of chemical vapor infiltration on erosion and thermal properties of porous carbon/carbon composite thermal insulation, *Carbon* 38 (3) (2000) 441–449.
- [2] B. Wicklein, A. Kocjan, G. Salazar-Alvarez, F. Carosio, G. Camino, M. Antonietti, L. Bergström, Thermally insulating and fire-retardant lightweight anisotropic foams based on nanocellulose and graphene oxide, *Nat. Nanotechnol.* 10 (2014) 277.
- [3] D.L. Schmidt, R.D. Craig, Advanced Carbon Fabric/Phenolics for Thermal Protection Applications, Air Force Wright Aeronautical Labs, Wright-Patterson Air Force Base, OH, 1982, No. AFWAL-TR-81-4136.
- [4] F. Panerai, J.C. Ferguson, J. Lachaud, A. Martin, M.J. Gasch, N.N. Mansour, Microtomography based analysis of thermal conductivity, diffusivity and oxidation behavior of rigid and flexible fibrous insulators, *Int. J. Heat Mass Transfer* 108 (2017) 801–811.
- [5] H. Tran, C. Johnson, D. Rasky, F. Hui, M.-T. Hsu, Y. Chen, Phenolic Impregnated Carbon Ablators (PICA) for discovery class missions, in: 31st Thermophysics Conference, American Institute of Aeronautics and Astronautics, 1996, AIAA Paper 1996-1911.
- [6] F.S. Milos, M.J. Gasch, D.K. Prabhu, Conformal phenolic impregnated carbon ablator arcjet testing, ablation, and thermal response, *J. Spacecraft Rock.* 52 (3) (2015) 804–812.
- [7] C. Szalai, E. Slimko, P. Hoffman, Mars science laboratory heatshield development, implementation, and lessons learned, *J. Spacecraft Rock.* 51 (4) (2014) 1167–1173.
- [8] D.A. Kontinos, M.J. Wright, Introduction: atmospheric entry of the stardust sample return capsule, *J. Spacecraft Rock.* 47 (5) (2010) 705–707.
- [9] R.A. Beck, D.M. Driver, M.J. Wright, H.H. Hwang, K.T. Edquist, S.A. Sepka, Development of the mars science laboratory heatshield thermal protection system, *J. Spacecraft Rock.* 51 (4) (2014) 1139–1150.
- [10] K.A. Trumble, I. Cozmuta, S. Sepka, P. Jenniskens, M. Winter, Postflight aerothermal analysis of the stardust sample return capsule, *J. Spacecraft Rock.* 47 (5) (2010) 765–774.
- [11] M. Gasch, M. Stackpoole, S. White, T. Boghazian, Development of advanced conformal ablative TPS fabricated from Rayon- and pan-based carbon felts, in: 57th AIAA/ASCE/AHS/ASC Structures, Structural Dynamics, and Materials Conference, American Institute of Aeronautics and Astronautics, 2016, AIAA Paper 2016-1414.
- [12] J.C. Ferguson, F. Panerai, J. Lachaud, A. Martin, S.C.C. Bailey, N.N. Mansour, Modeling the oxidation of low-density carbon fiber material based on microtomography, *Carbon* 96 (2016) 57–65.
- [13] P.R. Mahaffy, C.R. Webster, S.K. Atreya, H. Franz, M. Wong, P.G. Conrad, D. Harpold, J.J. Jones, L.A. Leshin, H. Manning, T. Owen, R.O. Pepin, S. Squyres, M. Trainer, Abundance and isotopic composition of gases in the martian atmosphere from the curiosity rover, *Science* 341 (6143) (2013) 263.
- [14] F.S. Milos, Y.K. Chen, Ablation predictions for carbonaceous materials using two databases for species thermodynamics, *J. Spacecraft Rock.* 50 (2) (2013) 245–255.
- [15] F.S. Milos, Y.-K. Chen, Ablation, thermal response, and chemistry program for analysis of thermal protection systems, *J. Spacecraft Rock.* 50 (1) (2013) 137–149.
- [16] M.E. Ewing, D.A. Isaac, Mathematical modeling of multiphase chemical equilibrium, *J. Thermophys. Heat Transfer* 29 (3) (2015) 551–562.
- [17] J. Lachaud, I. Cozmuta, N.N. Mansour, Multiscale approach to ablation modeling of phenolic impregnated carbon ablators, *J. Spacecraft Rock.* 47 (6) (2010) 910–921.
- [18] F.S. Milos, D.J. Rasky, Review of numerical procedures for computational surface thermochemistry, *J. Thermophys. Heat Transfer* 8 (1) (1994) 24–34.
- [19] W.E. Welsh Jr., P.M. Chung, A modified theory for the effect of surface temperature, in: Proceedings of the 1963 Heat Transfer and Fluid Mechanics Institute, Pasadena, CA, USA, 1963, pp. 146–159.
- [20] S.V. Zhukov, T. Abe, Viscous shock-layer simulation of airflow past ablating blunt body with carbon surface, *J. Thermophys. Heat Transfer* 13 (1) (1999) 50–59.
- [21] Y.-K. Chen, F.S. Milos, Navier-Stokes solutions with finite rate ablation for planetary mission earth reentries, *J. Spacecraft Rock.* 42 (6) (2005) 961–970.
- [22] M.A. Havstad, R.M. Ferencz, Comparison of surface chemical kinetic models for ablative reentry of graphite, *J. Thermophys. Heat Transfer* 16 (4) (2002) 508–515.
- [23] J. Marschall, M. MacLean, Finite-Rate Surface Chemistry Model, I: Formulation and reaction system examples, in: 42nd AIAA Thermophysics Conference, American Institute of Aeronautics and Astronautics, 2011, AIAA Paper 2011-3783.
- [24] M. MacLean, J. Marschall, D. Driver, Finite-rate surface chemistry model, II: Coupling to viscous Navier-Stokes code, in: 42nd AIAA Thermophysics Conference, American Institute of Aeronautics and Astronautics, 2011, AIAA Paper 2011-3784.
- [25] F.S. Milos, Y.-K. Chen, T. Gokcen, Nonequilibrium ablation of phenolic impregnated carbon ablator, *J. Spacecraft Rock.* 49 (5) (2012) 894–904.
- [26] H. Alkandry, I.D. Boyd, A. Martin, Coupled flow field simulations of charring ablators with nonequilibrium surface chemistry, in: 44th AIAA Thermophysics Conference, American Institute of Aeronautics and Astronautics, 2013, AIAA Paper 2013-2634.
- [27] C.R. Alba, R.B. Greendyke, J. Marschall, Development of a nonequilibrium finite-rate ablation model for radiating earth reentry flows, *J. Spacecraft Rock.* 53 (1) (2015) 98–120.
- [28] C.R. Alba, R.B. Greendyke, S.W. Lewis, R.G. Morgan, T.J. McIntyre, Numerical modeling of earth reentry flow with surface ablation, *J. Spacecraft Rock.* 53 (1) (2015) 84–97.
- [29] C.R. Alba, R.B. Greendyke, Nonequilibrium finite-rate carbon ablation model for earth reentry flows, *J. Spacecraft Rock.* 53 (3) (2016) 579–583.
- [30] G.V. Candler, C.R. Alba, R.B. Greendyke, Characterization of carbon ablation models including effects of gas-phase chemical kinetics, *J. Thermophys. Heat Transfer* 31 (2017) 512–526.
- [31] A. Borner, K. Swaminathan Gopalan, K.A. Stephani, V. Murray, S.J. Poovathingal, T. Minton, F. Panerai, N.N. Mansour, DSMC analysis of molecular beam experiments on light-weight carbon preform ablators, in: 47th AIAA Thermophysics Conference, American Institute of Aeronautics and Astronautics, 2017, AIAA Paper 2017-3687.
- [32] K. Swaminathan Gopalan, A. Borner, K.A. Stephani, V. Murray, S.J. Poovathingal, T. Minton, N.N. Mansour, DSMC analysis of molecular beam experiments for oxidation of carbon based ablators, in: 55th AIAA Aerospace Sciences Meeting, American Institute of Aeronautics and Astronautics, 2017, AIAA Paper 2017-1845.
- [33] S.J. Poovathingal, T.E. Schwartzentruber, V. Murray, T.K. Minton, G.V. Candler, Finite-rate oxidation model for carbon surfaces from molecular beam experiments, *AIAA J.* 55 (5) (2017) 1644–1658.
- [34] K. Swaminathan Gopalan, K.A. Stephani, Construction of finite rate surface chemistry models from molecular beam experimental data, in: 47th AIAA Thermophysics Conference, American Institute of Aeronautics and Astronautics, 2017, AIAA Paper 2017-4347.
- [35] K. Swaminathan-Gopalan, A. Borner, V.J. Murray, S. Poovathingal, T.K. Minton, N.N. Mansour, K.A. Stephani, Development and validation of a finite-rate model for carbon oxidation by atomic oxygen, *Carbon* 137 (2018) 313–332.
- [36] P. Schrooyen, K. Hillewaert, T.E. Magin, P. Chatelain, Fully implicit Discontinuous Galerkin solver to study surface and volume ablation competition in atmospheric entry flows, *Int. J. Heat Mass Transfer* 103 (2016) 108–124.

- [37] J. Lachaud, N. Bertrand, G.L. Vignoles, G. Bourget, F. Rebillat, P. Weisbecker, A theoretical/experimental approach to the intrinsic oxidation reactivities of C/C composites and of their components, *Carbon* 45 (14) (2007) 2768–2776.
- [38] J.R. Arthur, Reactions between carbon and oxygen, *Trans. Faraday Soc.* 47 (1951) 164–178.
- [39] P.L. Walker, F. Rusinko, L.G. Austin, Gas reactions of carbon, in: D.D. Eley, P.W. Selwood, P.B. Weisz (Eds.), *Advances in Catalysis*, Academic Press, 1959, pp. 133–221.
- [40] E. Gulbransen, K. Andrew, F. Brassart, The oxidation of graphite at temperatures of 600 to 1500 C and at pressures of 2 to 76 torr of oxygen, *J. Electrochem. Soc.* 110 (6) (1963) 476–483.
- [41] E.A. Gulbransen, High-temperature oxidation of tungsten, molybdenum and carbon, *Nature* 198 (4875) (1963) 82–83.
- [42] D. Rosner, H. Allendorf, High temperature oxidation of carbon by atomic oxygen, *Carbon* 3 (2) (1965) 153–156.
- [43] H. Allendorf, D. Rosner, High-temperature kinetics of graphite oxidation by dissociated oxygen, *AIAA J.* 3 (8) (1965) 1522–1523.
- [44] H.D. Allendorf, D.E. Rosner, Comparative studies of the attack of pyrolytic and isotropic graphite by atomic and molecular oxygen at high temperatures, *AIAA J.* 6 (4) (1968) 650–654.
- [45] V.Z. Shemet, A.P. Pomytkin, V.S. Neshpor, High-temperature oxidation behaviour of carbon materials in air, *Carbon* 31 (1) (1993) 1–6.
- [46] J. Marschall, M. MacLean, P.E. Norman, T.E. Schwartzentruber, Surface Chemistry in Non-Equilibrium Flows, *Hypersonic Nonequilibrium Flows: Fundamentals and Recent Advances*, American Institute of Aeronautics and Astronautics, 2015, pp. 239–327.
- [47] F. Panerai, A. Martin, N.N. Mansour, S.A. Sepka, J. Lachaud, Flow-tube oxidation experiments on the carbon preform of a phenolic-impregnated carbon ablator, *J. Thermophys. Heat Transfer* 28 (2) (2014) 181–190.
- [48] J. Lachaud, N. Mansour, A. Ceballos, D. Pejakovic, L. Zhang, J. Marschall, Validation of a volume-averaged fiber-scale model for the oxidation of a carbon-fiber preform, in: 42nd AIAA Thermophysics Conference, American Institute of Aeronautics and Aerospace, 2011, AIAA Paper 2011–3640.
- [49] R. Jambunathan, D.A. Levin, A. Borner, J.C. Ferguson, F. Panerai, Prediction of gas transport properties through fibrous carbon preform microstructures using Direct Simulation Monte Carlo, *Int. J. Heat Mass Transfer* 130 (2019) 923–937.
- [50] N. Nouri, F. Panerai, K.A. Tagavi, N.N. Mansour, A. Martin, Evaluation of the anisotropic radiative conductivity of a low-density carbon fiber material from realistic microscale imaging, *Int. J. Heat Mass Transfer* 95 (2016) 535–539.
- [51] F. Panerai, J.D. White, T.J. Cochell, O.M. Schroeder, N.N. Mansour, M.J. Wright, A. Martin, Experimental measurements of the permeability of fibrous carbon at high-temperature, *Int. J. Heat Mass Transfer* 101 (2016) 267–273.
- [52] J. Marschall, F.S. Milos, Gas permeability of rigid fibrous refractory insulations, *J. Thermophys. Heat Transfer* 12 (4) (1998) 528–535.
- [53] A.D. Omidy, F. Panerai, J.R. Lachaud, N.N. Mansour, A. Martin, Effects of water phase change on the material response of low-density carbon-phenolic ablators, *J. Thermophys. Heat Transfer* 30 (2) (2016) 473–478.
- [54] A. Borner, F. Panerai, N.N. Mansour, High temperature permeability of fibrous materials using direct simulation Monte Carlo, *Int. J. Heat Mass Transfer* 106 (2017) 1318–1326.
- [55] F. Panerai, A. Martin, J. Lachaud, N.N. Mansour, Experimental and numerical study of carbon fiber oxidation, 52<sup>nd</sup> AIAA Aerospace Sciences Meeting, American Institute of Aeronautics and Astronautics, 2014, AIAA Paper 2014–1208.
- [56] H. Weng, A. Martin, Development of a universal solver and its application to ablation problems, in: 47th AIAA Thermophysics Conference, American Institute of Aeronautics and Astronautics, 2017, AIAA Paper 2017–3355.
- [57] V.K. Shen, D.W. Siderius, W.P. Krekelberg, H.W. Hatch, NIST Standard Reference Simulation Website, NIST Standard Reference Database Number 173, National Institute of Standards and Technology, Gaithersburg MD, 20899, 2016.
- [58] J.C. Ferguson, F. Panerai, J. Lachaud, N.N. Mansour, Theoretical study on the micro-scale oxidation of resin-infused carbon ablators, *Carbon* 121 (Supplement C) (2017) 552–562.
- [59] S.C.C. Bailey, D. Bauer, F. Panerai, S.C. Splinter, P.M. Danehy, J.M. Hardy, A. Martin, Experimental analysis of spallation particle trajectories in an arc-jet environment, *Exp. Therm. Fluid Sci.* 93 (2018) 319–325.
- [60] B. Marchon, J. Carrazza, H. Heinemann, G. Somorjai, TPD and XPS studies of O<sub>2</sub>, CO<sub>2</sub>, and H<sub>2</sub>O adsorption on clean polycrystalline graphite, *Carbon* 26 (4) (1988) 507–514.
- [61] M. Geier, C.R. Shaddix, F. Holzleithner, A mechanistic char oxidation model consistent with observed CO<sub>2</sub>/CO production ratios, *Proc. Combust. Inst.* 34 (2) (2013) 2411–2418.
- [62] P. Walker, R. Taylor, J. Ranish, An update on the carbon-oxygen reaction, *Carbon* 29 (3) (1991) 411–421.
- [63] J. Hunt, A. Ferrari, A. Lita, M. Crosswhite, B. Ashley, A. Stiegman, Microwave-specific enhancement of the carbon-carbon dioxide (Boudouard) reaction, *J. Phys. Chem. C* 117 (51) (2013) 26871–26880.
- [64] B. Marchon, W. Tysoe, J. Carrazza, H. Heinemann, G. Somorjai, Reactive and kinetic properties of carbon monoxide and carbon dioxide on a graphite, *J. Phys. Chem.* 92 (20) (1988) 5745.
- [65] G.S. Szymański, Z. Karpiński, S. Biniak, A. Świątkowski, The effect of the gradual thermal decomposition of surface oxygen species on the chemical and catalytic properties of oxidized activated carbon, *Carbon* 40 (14) (2002) 2627–2639.
- [66] U. Zielke, K. Hüttinger, W. Hoffman, Surface-oxidized carbon fibers: I. Surface structure and chemistry, *Carbon* 34 (8) (1996) 983–998.